Article:
Gunaydin, K. orcid.org/0000-0002-3045-130X, Kundakcıoğlu, E., Gülcan, O. et al. (1 more author) (2025) Shrink line formation in laser powder bed fusion process: an experimental and numerical study. The International Journal of Advanced Manufacturing Technology, 139 (9-10). pp. 5079-5093. ISSN: 0268-3768

https://doi.org/10.1007/s00170-025-16187-2

Shrink line formation in laser powder bed fusion process: an experimental and numerical study

Kadir Gunaydin[1*], Erdem Kundakcıoğlu, Orhan Gülcan, Evren Yasa[2]

[1]General Electric Aerospace, Kartal, Turkey, kadir.gunaydin@geaerospace.com; erdem.kundakcioglu@ge.com; orhan.gulcan@ geaerospace.com

[2]Advanced Manufacturing Research Centre, The University of Sheffield, Sheffield, UK, e.yasa@amrc.co.uk

Abstract

Shrink line formation is a phenomenon commonly observed, particularly at sharp cross-sectional area changes in metal parts produced using the Powder Bed Fusion Laser Beam (PBF-LB/M) additive manufacturing process. These lines negatively impact the part's appearance, dimensional accuracy, and fatigue life. This study focused on shrink line formation in specimens featuring hole patterns in both horizontal and vertical directions, manufactured using PBF-LB/M with Inconel 718 powder material. Experimental results revealed that shrink lines formed at the upper layer of the holes, where cross-sectional area changes reached up to 15% between successive layers. Thermomechanical finite element method (FEM) simulations were also conducted, demonstrating that shrink lines can be predicted through process simulation. This prediction was enabled by using an appropriate voxel element size, determined through a mesh convergence study. Voxel elements were employed as they are a powerful tool for discretizing and analyzing three-dimensional volumes, offering a balance between computational efficiency and the ability to model complex internal behaviors. The shrink line height from the bottom of the parts and their depth were predicted with error margins of 0.4% and 14%, respectively. Finally, microhardness and microstructure evaluations were performed, revealing that microhardness at shrink line locations was lower than in the surrounding areas.

Keywords: shrink line, laser powder bed fusion, patterned feature, process simulation

1. Introduction

Due to the increasing demand for lighter components, particularly in the aerospace and automotive industries, additive manufacturing (AM) technologies have garnered significant

attention in recent years. AM technologies not only enable the production of complex and lightweight components without the need for process tools but also offer reduced process times [1]. In the described manufacturing technique, a laser serves as a key tool to precisely melt metal powder. As the laser moves across the powder bed, it fuses the metal particles together layer by layer. This layer-by-layer accumulation facilitates the creation of complex three-dimensional geometries. Each layer solidifies upon cooling, bonding with the layer beneath it, and gradually builds the object in a precise and controlled manner. This process is revolutionary in the field of manufacturing, as it enables the production of parts and components with intricate designs that would be challenging, if not impossible, to achieve using traditional manufacturing methods [2, 3].

Despite the advantages of the Powder Bed Fusion of Metals using a Laser Beam (PBF-LB/M) process, such as the ability to manufacture complex parts with shorter lead times, it has certain drawbacks. PBF-LB/M parts often exhibit surface, sub-surface, or internal defects that limit the process in terms of part quality, repeatability, and final mechanical properties [4]. Lack of fusion and porosities are among the defects commonly observed in PBF-LB/M manufactured parts [5]. Beyond these defects, the localized melting caused by the laser in the PBF-LB/M process results in significant temperature gradients within the material [6]. These gradients, in turn, lead to substantial thermally induced residual stresses. Furthermore, these stresses can cause distortion in the parts being manufactured [7]. This phenomenon occurs because the rapid heating and cooling associated with the laser melting process create uneven expansion and contraction within the material, resulting in internal stresses and, consequently, distortion of the final product [8].

Particularly at points where there is a transition to a larger cross-section in the structure or vice versa along the build direction, localized deformation occurs on the outer surface of the part, resulting in notch formation. The notch formation observed on the surface of produced parts is referred to as the shrink line (Figure 1), and two distinct mechanisms contribute to its root cause. One mechanism is associated with the stoppage or pause in the build process, during which the deposited layer cools down, altering the thermal history at a local layer [9]. The second mechanism is more closely related to the geometrical features of the built part.

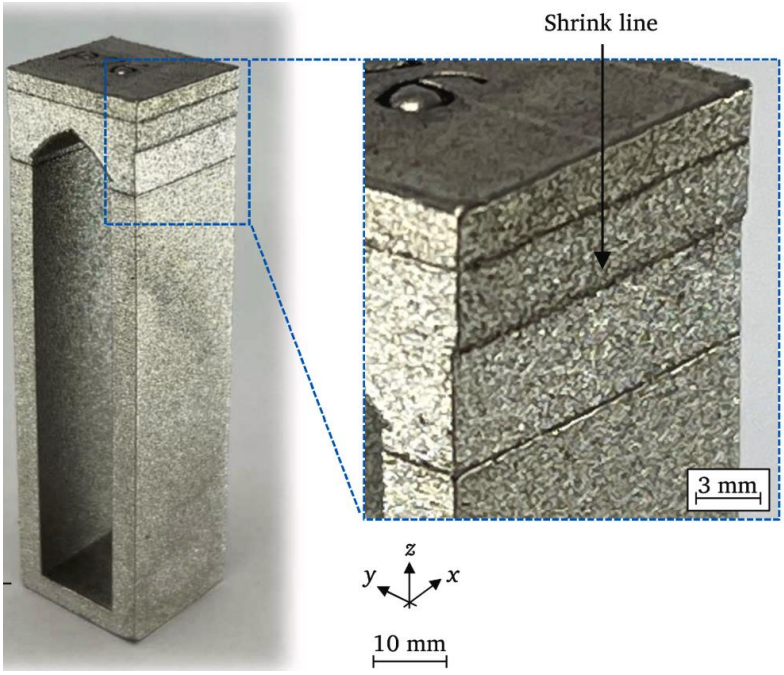

Figure 1. An example of shrink line in PBF-LB/M process [10]

During the PBF-LB/M process, if there are instant and drastic changes in cross-sectional area between successive layers in the part, local deformations may occur on the outer surfaces due to thermal gradients between layers, further contributing to changes in the thermal history. These deformations may form a notch called a shrink line, which affects the dimensional accuracy and fatigue life of the specimens by initiating cracks [11]. Shrink lines are formed after the first few slices of structural transition zones, meaning they are parallel to the build platform. Rauner et al.'s experimental investigation revealed that shrink line formation is primarily caused by local overheating at the structural transition and the global cooling behavior [10]. Shrink lines impact the part on two different scales: they affect local warping at the level of individual layers, known as the mesoscale, and they also influence the overall warping of the entire structure, referred to as the macroscale. This means that shrink lines not only cause distortions in the layer-by-layer construction of the part but also contribute to larger, overall deformation of the geometry of the part. Consequently, shrink lines pose a considerable challenge by diminishing the dimensional accuracy of parts. This reduction in precision necessitates a greater amount of post-processing work to correct these inaccuracies and meet the required specifications [12]. Therefore, Adam and Zimmer [13] advise against incorporating significant structural transitions in the design that involve an increase in cross-section. The increased cross-section results in the accumulation of heat due to a greater quantity of thermal energy being produced. However, completely avoiding structural transitions in

topology-optimized geometries is not always feasible, as doing so would limit design freedom. Kranz [14] indicated that shrink lines occur at structural transitions due to the volume contraction of individual layers. These layers are formed over an area of unsolidified powder beneath them. The thermal contraction results in tensile forces being exerted within the structure in the direction of printing, leading to distortion and the formation of a notch on the external surface of the structure. The presence of the notch could heighten the risk of crack formation, thereby potentially decreasing the life of the part. Goetz et al. [11] developed a method for measuring shrink lines and categorized the shape of the resulting notch into four separate areas. Additionally, they measured the size of a shrink line across different radii at the structural transition point. Their findings indicated that the deepest shrink line observed in the examined geometries was 150 ± 13 micrometers. In another study, Goetz et al. [15] investigated how these notches affect fatigue resistance. A typical shrink line was incorporated into a standard test sample, with the notch depth of the shrink line varying from 0 to 300 μm. The shrink lines, as they were initially made, were measured using optical methods. Additionally, the material's resistance to fatigue under dynamic loading conditions and the characteristics of the fracture surfaces were studied. The results indicated that shrink lines influence fatigue resistance in a manner comparable to basic notch shapes. Rauner et al. proposed an algorithm to effectively predict shrink line locations in the PBF-LB/M process, which characterizes the area, perimeter, and centroids of successive layers [16]. Gülcan et al. [17] investigated shrink line formation in triply periodic minimal surfaces (TPMS) lattices produced by the PBF-LB/M process using thermomechanical simulations and stated that Primitive lattices are more prone to shrink line formation than Gyroid and Diamond lattices.

Some studies in the existing literature have been dedicated to investigating the impact of shrink lines on the fatigue life of parts and the methods for the dimensional characterization of shrink lines formed due to machine stoppage [9]. However, in some studies, shrink lines were observed but not included in fatigue assessments [18]. Additionally, various research studies in the literature have focused on establishing design guidelines for the PBF-LB/M process using different materials, such as Ti6Al4V [19], In718 [20], and metal foam [21]. However, these guidelines do not provide specific recommendations for preventing or reducing shrink line formation. Moreover, to the best of the authors' knowledge, no study has yet focused on investigating shrink line formation in structures with staggered holes or identifying threshold values above which structures become more prone to shrink line formation. To address this gap, the present study experimentally and numerically investigates shrink line formation

caused by instant and drastic changes in cross-sectional area between successive layers in the part.

In this study, the production of parts with repeated cross-sectional area changes between successive layers was examined to demonstrate the formation of shrink lines. The dimensional characteristics of shrink lines were investigated using an optical profilometer. Furthermore, a thermomechanical Finite Element Method (FEM) model was developed to simulate shrink line formation, and the simulation results were validated against experimental outcomes. Additionally, an analytical method was proposed as a design tool to predict the formation of shrink lines.

2. Materials and Methods

2.1.Specimen Design and Build Preparation

Figure 2 illustrates the specimen geometry and general dimensions used in the present study. Siemens NX 12 software (Siemens AG, Germany) was utilized to generate the geometry. According to the literature, any hole with a diameter larger than 12 mm typically requires support structures [19]. Therefore, in this study, 6 mm diameter holes were used to avoid the need for support structures within the holes. To ensure the repeatability of the assessments for each specimen, 4-hole patterns were employed in both axial and vertical directions. A 2 mm bottom stock was added to all geometries to facilitate the separation of parts from the build platform via wire electrical discharge machining. Five specimens were positioned on the build platform, as shown in Figure 3, where the directions for powder recoating and gas flow (aligned with the recoater direction, -x direction) are indicated by a black arrow. The specimens were symmetrically arranged along the x and y axes, spaced 8 mm apart from each other, and oriented at a 5° angle with respect to the recoater direction. Along the x direction, the two side surfaces of the specimens were designated as the front (S1) and back (S2) surfaces, where the front surface is closer to the start of the recoater blade, and the back surface is farther away.

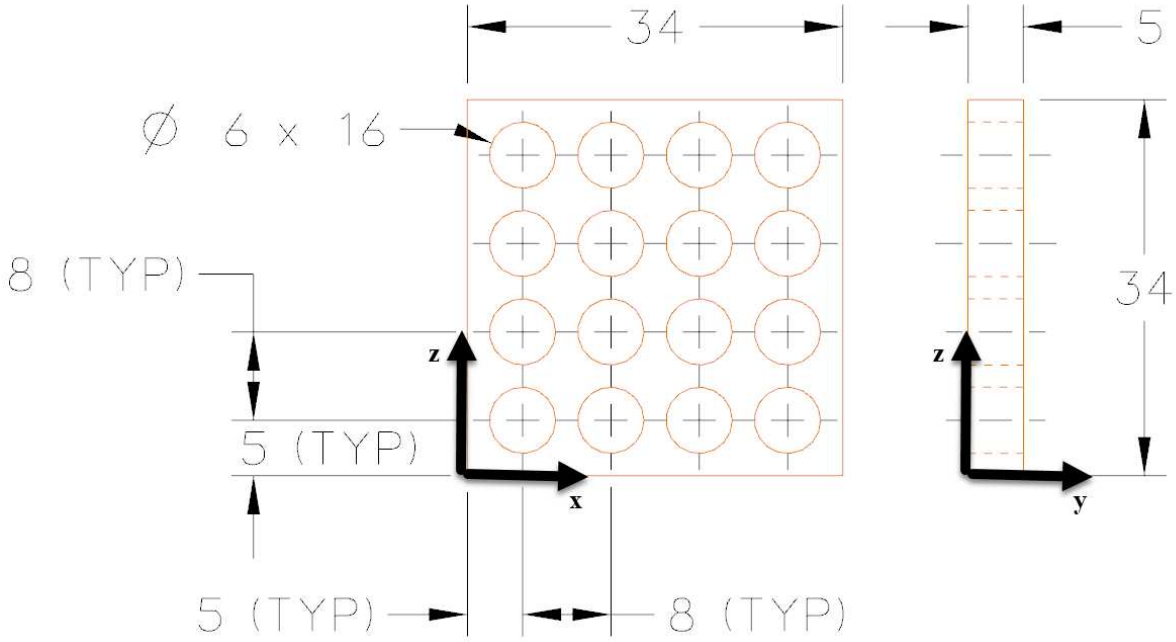

Figure 2. The geometry and general dimensions (in mm)

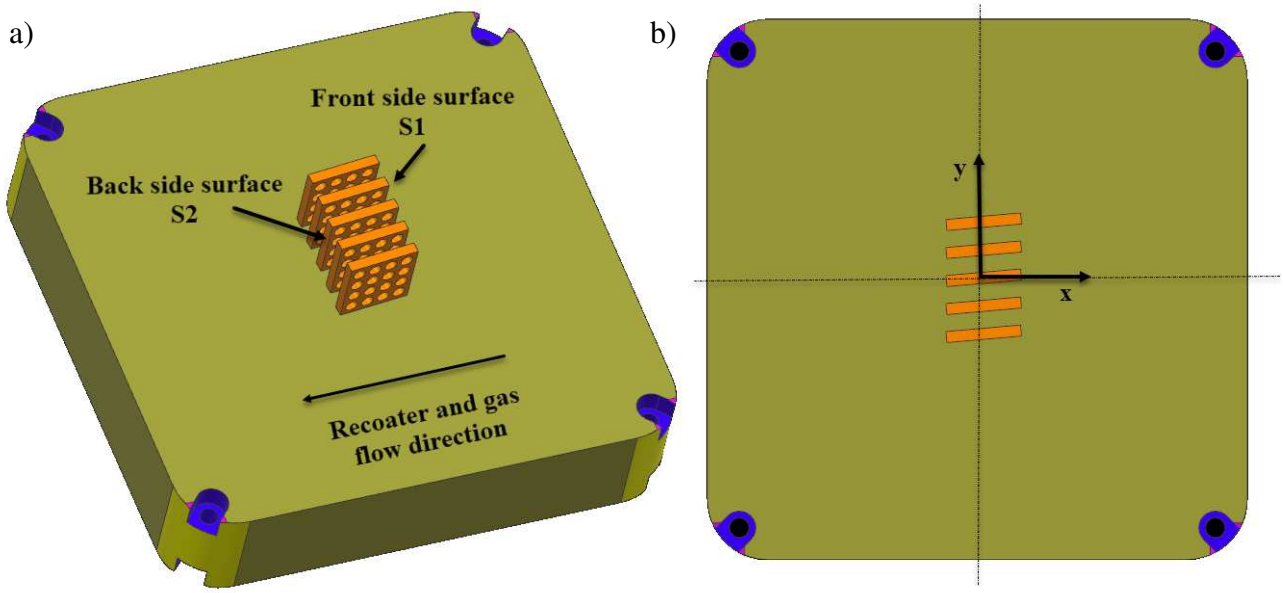

Figure 3. Build platform and layout, a) perspective view, b) top view

2.2. Build and Measurements

The specimens were manufactured using gas-atomized spherical Inconel 718 powder material (GE Additive, Mölnlycke, Sweden) on a Concept Laser M2 PBF-LB/M machine (Concept Laser GmbH, GE Additive, Germany) under a nitrogen gas environment. The process parameters included 160 W laser power, 680 mm/s laser scanning speed, 53 µm laser spot size,

100 μm hatch spacing, and 50 μm layer thickness. After manufacturing, the powder evacuation process was performed using a Solukon SFM-AT800 system (Solukon Maschinenbau GmbH, Augsburg, Germany). The specimens were then removed from the build platform using a GF Agiecharmilles wire electrical discharge machine (Agie Charmilles Ltd., Switzerland) and scanned with an Alicona InfiniteFocus G5 optical profilometer (Alicona Imaging GmbH, Graz, Austria). During optical scanning, 10X magnification, polarized coaxial illumination, 6 μm lateral resolution, and 900 nm vertical resolution were used. Alicona MeasureSuite 5.3.6 – ProfileFormMeasurement software was employed to measure the shrink line heights and depths. To measure the shrink line characteristics, the lateral sides of the coupons were scanned with the optical profilometer, and surface profiles were extracted along a vertical line at the mid-plane of the lateral surfaces (see Figures 8 and 9). To investigate the microstructural changes at, below, and above the shrink line areas, the specimens were cut along their center plane using a Struers Secotom cutter, mounted in a Struers CitoPress mounting machine, and polished with a Struers Tegramin system (Struers LLC, Ohio, US). Metallographic studies were conducted using a Zeiss Merlin FE-SEM scanning electron microscope (Carl Zeiss AG, Jena, Germany). Hardness measurements at, below, and above the shrink line areas were performed using an Emco-Test DuraScan-70 microhardness tester (EMCO-TEST Prüfmaschinen GmbH, Kuchl, Austria) with the Vickers hardness scale 0.3 (HV 0.3, 2.942 N).

2.3. Simulations

During the thermal process of PBF-LB/M, the laser beam scans and melts the powder, and the molten material cools down and contracts, resulting in residual stress within the part. This residual stress can lead to surface issues, geometric accuracy problems, and, in some cases, build failures. To predict these issues, thermal and mechanical simulation-based finite element modeling can be employed, which helps reduce the cost associated with trial-and-error printing [22].

For the thermomechanical numerical analysis of the PBF-LB/M process, Simufact Additive 4.1 commercial software (Simufact Engineering GmbH, Germany) was utilized. Simufact operates on a decoupled thermomechanical finite element modeling approach, where a thermal history is first obtained through thermal simulation and then used as boundary conditions in the mechanical model. To obtain mechanical results, the software employs the inherent strain method, which uses plastic strain data acquired from printed strain calibration coupons [23].

The Simufact Material Library was used, and Inconel 718 powder was selected as the powder material. Build platform distortion was not considered in the simulation. The build platform (AISI 316L stainless steel with dimensions of 245x245x50 mm) and specimens were discretized using voxel elements. To determine the optimal voxel element size, a mesh convergence study was conducted for the as-built and immediate release states. For this purpose, voxel element sizes of 1.2, 1.0, 0.8, 0.6, 0.4, 0.2, and 0.1 mm were tested, and the maximum total displacement and maximum Von Mises stress values were measured for both states. The effects of voxel element size on maximum Von Mises stress values are presented in Figure 4. Since the as-built and immediate release values for maximum Von Mises stresses converge closely at a voxel element size of 0.1 mm, this size was selected for the present study. The corresponding meshed geometry with 0.1 mm voxel elements is shown in Figure 5. The total simulation time on a workstation was 6.5 hours to complete.

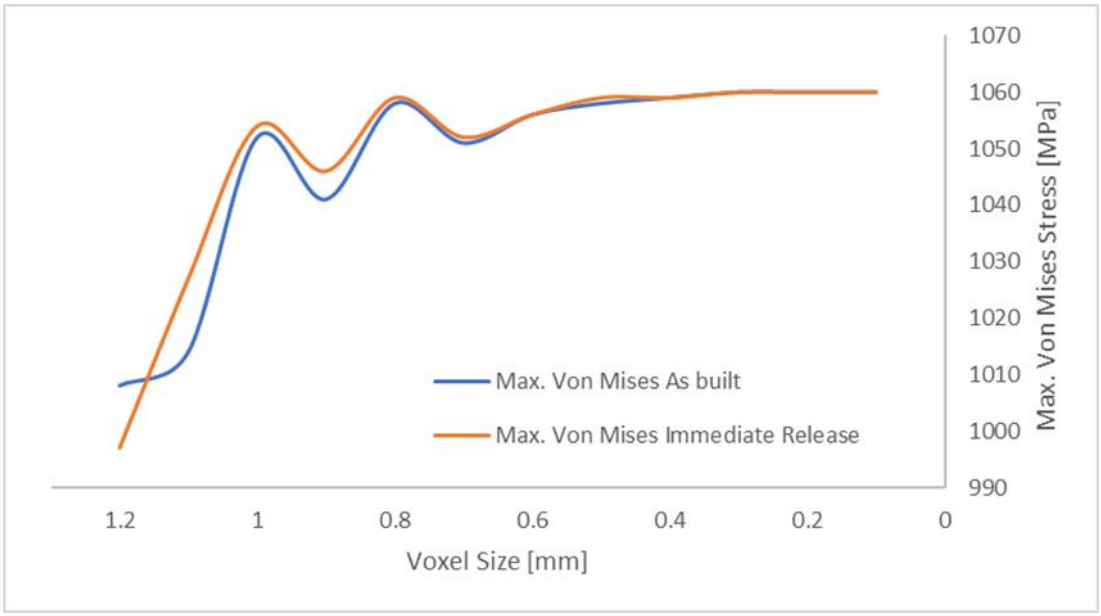

Figure 4. The effect of voxel element size on maximum Von Mises stress

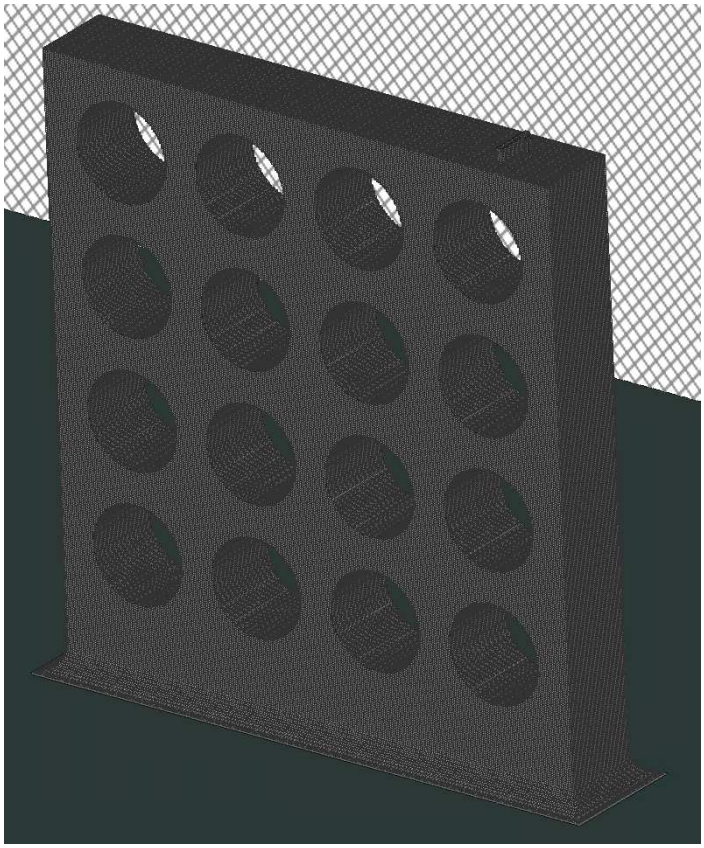

Figure 5. The geometry with 0.1 mm voxel elements used for simulation

The displacement along the X-axis was considered for shrink line comparison because it corresponds to the depth of the shrink line. Data points were collected from each side wall along a line, and the methodology for obtaining simulation data points is illustrated in Figure 6.

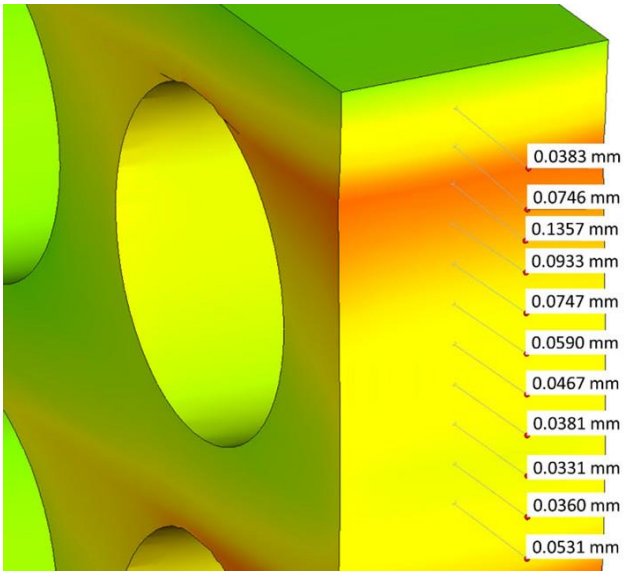

Figure 6. The methodology of obtaining simulation data points (S1)

3. Results and Discussions

3.1. Optical Profilometer Measurement Results

As part of the experimental group, five specimens were manufactured, and no failures or issues were observed except for shrink lines upon visual inspection. Figure 7 shows an image of one representative produced part, where surface irregularities in the overhang regions of the specimen are clearly visible. Sagging melt pools and the adhesion of partially melted powder particles to the surface are the two most significant factors contributing to the high surface roughness values observed in these areas [24, 25]. These surface irregularities play a critical role in determining the mechanical properties of the final component [26, 27]. It is evident from Figure 7 that the overhang surfaces of the holes sag towards the bottom, opposite to the build direction.

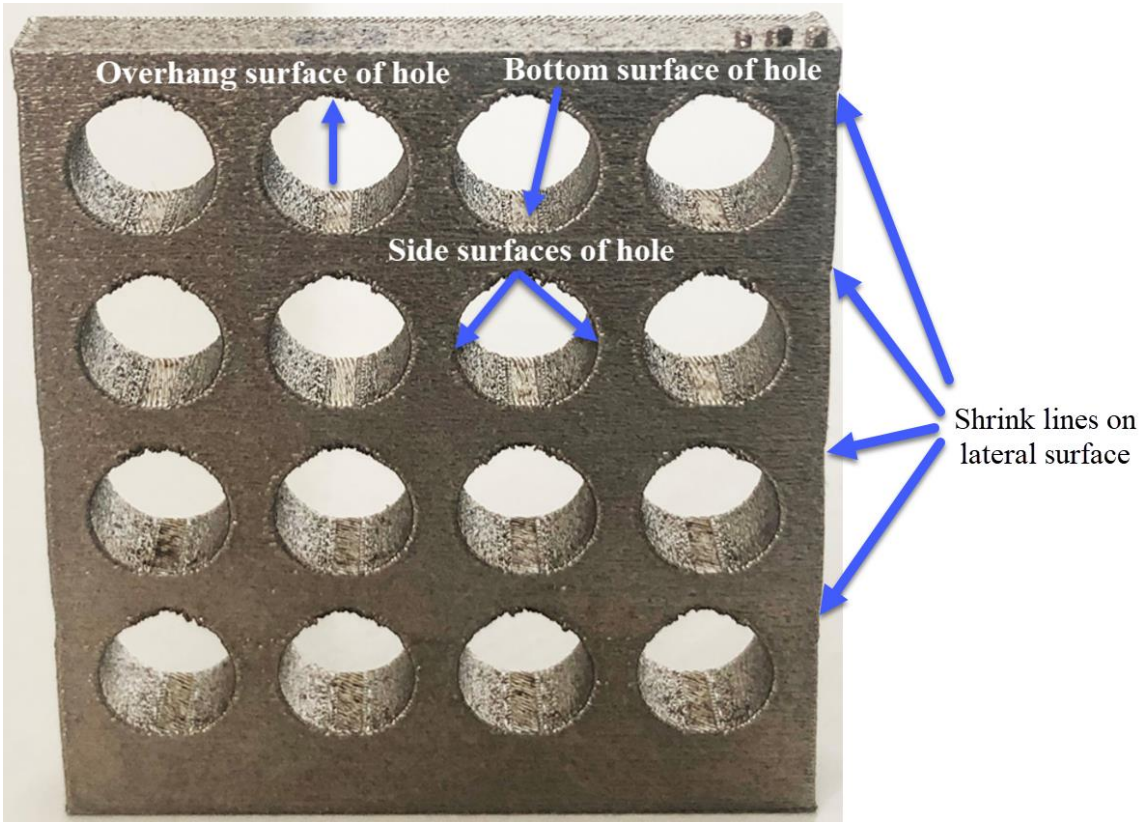

Figure 7. Produced specimen

Optical profilometer images of the lateral side surfaces, running from bottom to top, are shown in Figure 8. S1 and S2 represent the side walls located close to and away from the recoater

direction, respectively. Four distinct shrink lines were observed and are indicated in Figure 8 with blue arrows. The z-height of these shrink lines, measured from the bottom of the specimens, was recorded, and the results are presented in Figures 9 and 10.

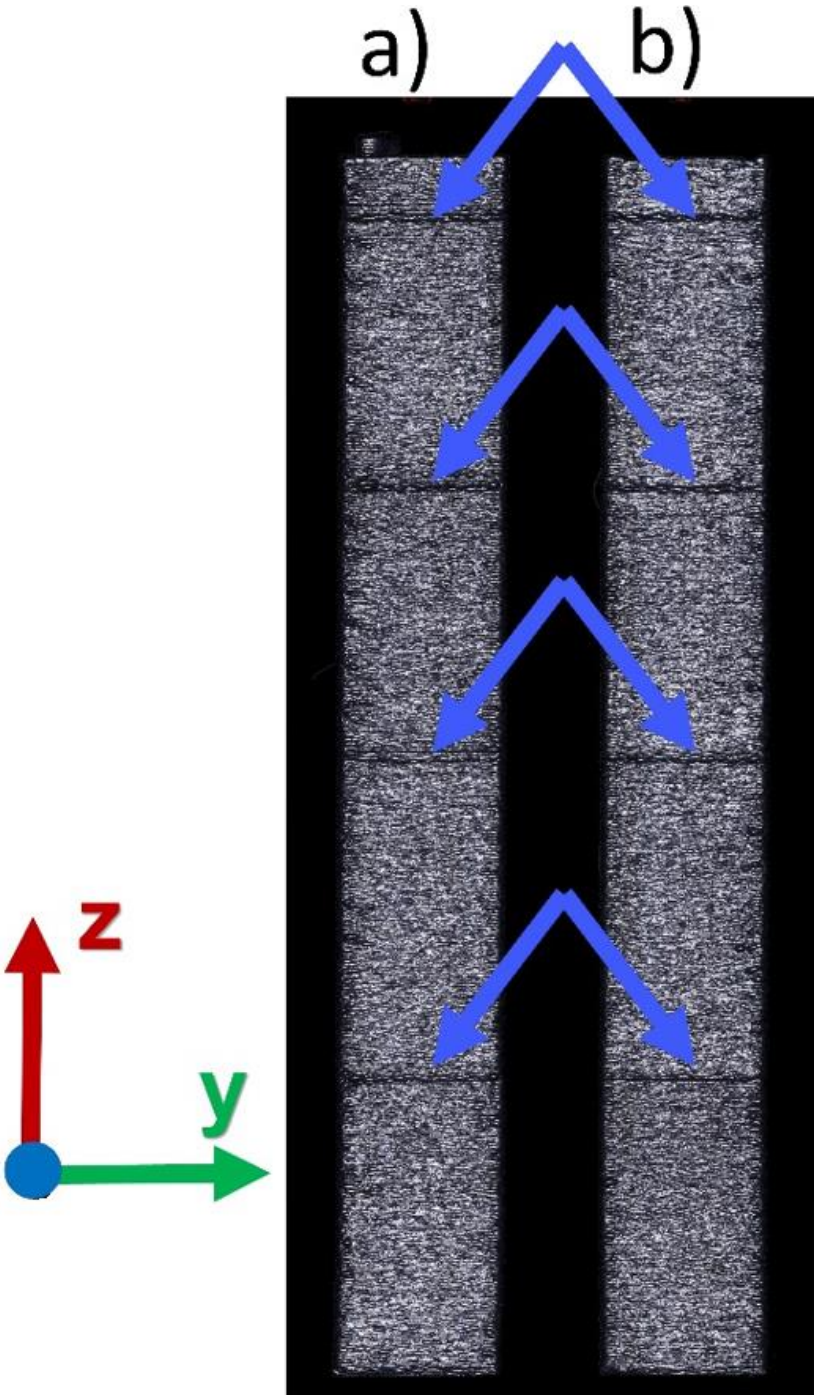

Figure 8. Optical profilometer pictures from a) front sidewall (S1), b) back sidewall (S2) of specimen #2. Blue arrows show the shrink lines

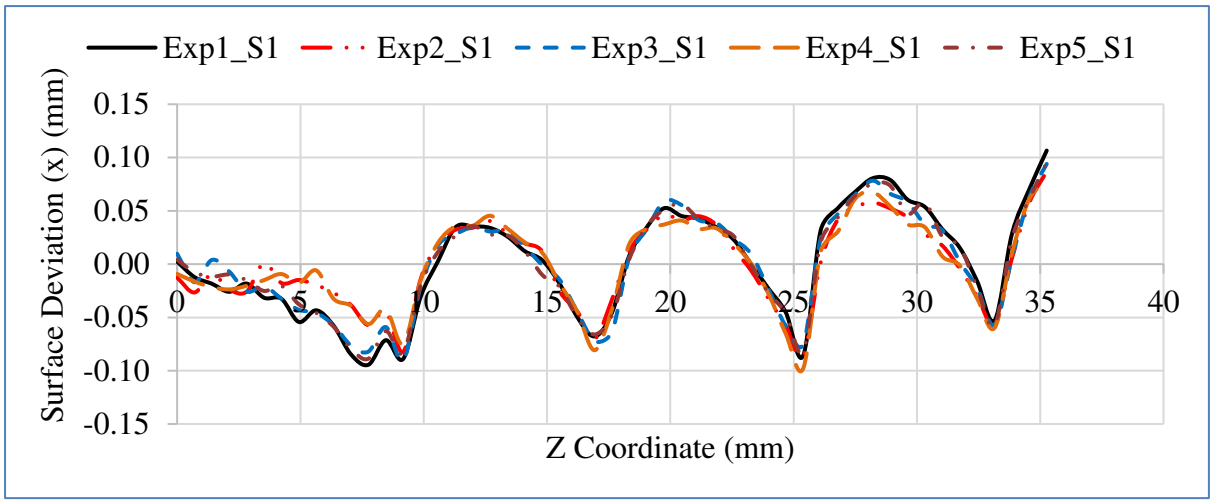

Figure 9. Shrink line measurements of the front sidewall (S1) of the five builds

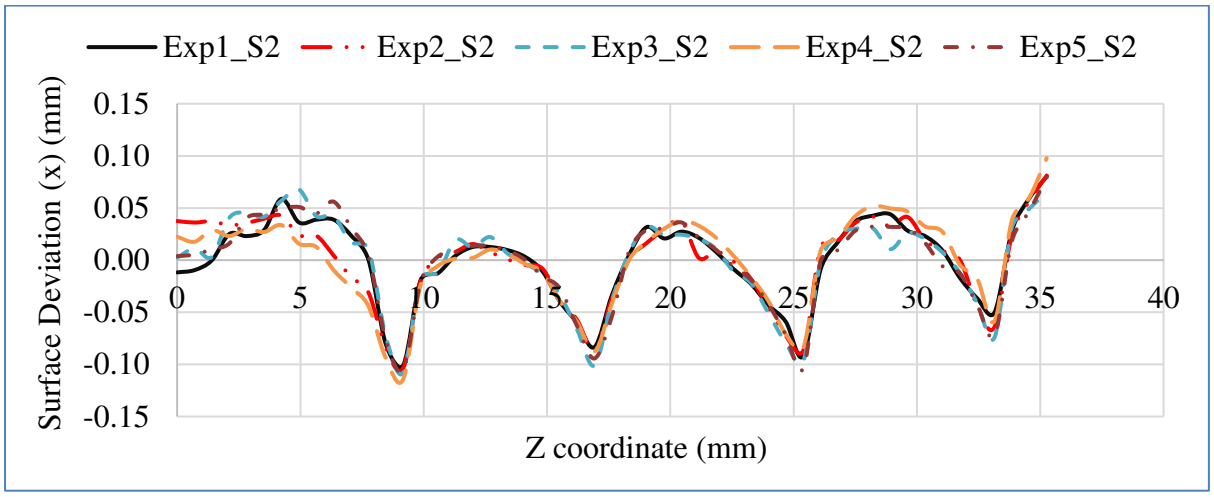

Figure 10. Shrink line measurements of the back sidewall (S2) of the five builds

The depth of the shrink lines was calculated by subtracting the surface deviation value of the shrink line from the surfaces above the shrink lines (Figure 11). In other words, the depth of the shrink lines was measured by using the sidewall surfaces as reference surfaces. The depth of the shrink lines for both sidewalls of the five builds is presented in Tables 1 and 2. The deviation of the measured shrink line depths on the front sidewall (S1) from the average values ranges from -8.9% to 7.4%, while the deviation on the back sidewall (S2) ranges from -10.3% to 8.1%. The depth of the shrink lines increases in accordance with the z-height of the shrink lines. This can be attributed to the fact that at locations further away from the base plate, geometrical changes play a more significant role in shrink line formation, as they are primarily responsible for altering the thermal gradients. However, near the base plate, the effect of cross-

sectional area changes on shrink line formation diminishes, as the base plate acts as a heat sink, directly influencing the thermal gradients along with the geometrical changes.

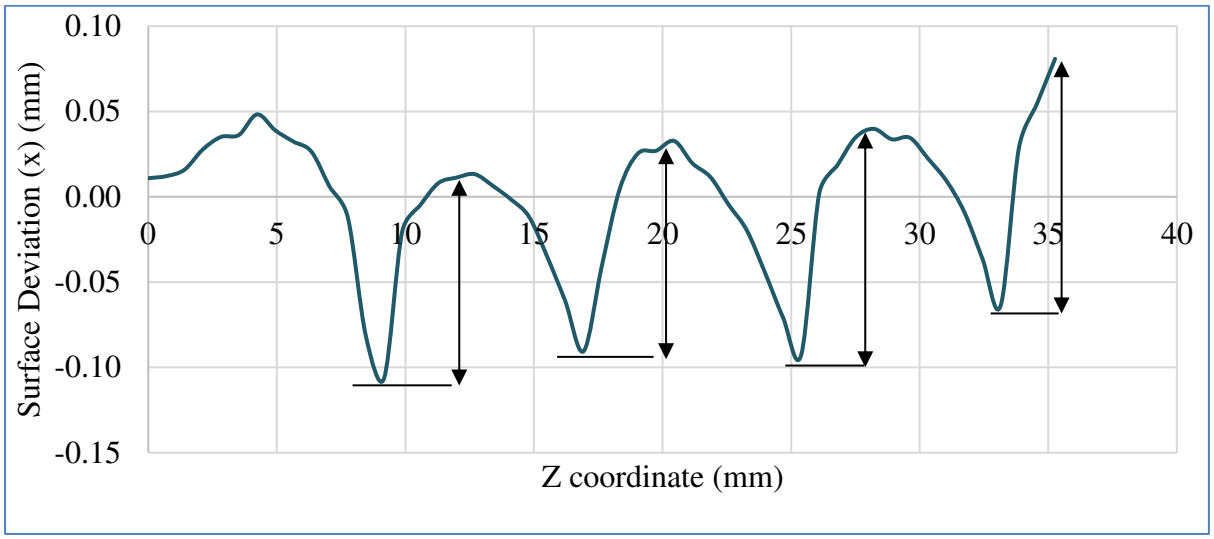

Figure 11. Methodology for shrink line depth calculation

Table 1. Shrink line depth measurements for the front sidewall (S1). Values are in mm.

Experiment No	Shrink Line#1	Shrink Line#2	Shrink Line#3	Shrink Line#4
Experiment#1	0.124	0.120	0.166	0.160
Experiment#2	0.123	0.116	0.143	0.144
Experiment#3	0.125	0.128	0.153	0.151
Experiment#4	0.120	0.122	0.165	0.137
Experiment#5	0.119	0.122	0.157	0.153
Experiment_Avg	0.120	0.121	0.157	0.149

Table 2. Shrink line depth measurements for the back sidewall (S2). Values are in mm.

Experiment No	Shrink Line#1	Shrink Line#2	Shrink Line#3	Shrink Line#4
Experiment#1	0.113	0.115	0.136	0.130
Experiment#2	0.119	0.124	0.129	0.145
Experiment#3	0.127	0.133	0.128	0.139
Experiment#4	0.124	0.121	0.136	0.156
Experiment#5	0.120	0.130	0.136	0.152
Experiment_Avg	0.120	0.123	0.133	0.145

The height of the shrink lines in the z-direction for the front and back sidewalls was measured relative to the bottom plane of the specimens using an optical profilometer, and the results are provided in Table 3 for specimen #2. No deviation in the measured shrink line z-heights for the front sidewall (S1) and back sidewall (S2) was observed. All test data indicated that the z-height of the shrink lines remains consistent across the same z-height. Additionally, by comparing the shrink line depths at the same z-heights between the front and back side surfaces, as shown in Tables 1 and 2, it can be observed that the shrink line depths alternate between -1.65% and 15% on opposite sidewalls. Furthermore, the shrink lines on the front sidewalls, which are in the first recoater interaction direction, exhibit slightly higher values.

Table 3. Shrink line z-heights from bottom surface for the S1 and S2

Experiment No	Shrink Line#1	Shrink Line#2	Shrink Line#3	Shrink Line#4
z-height (mm)	9.169	16.927	25.390	33.148

It is mentioned in the literature [28, 29] that laser scanning has an annealing effect on previous layers. However, due to the drastic increase in cross-sectional area and low heat conduction, the residual stress in the upper portion of the hole (Figure 12(a)) is not relieved. Consequently, during cooling and contraction, the upper portion of the hole geometry distorts inward. This distortion can lead to shrink line formation at the top of the hole, as illustrated in Figure 12(b) [30].

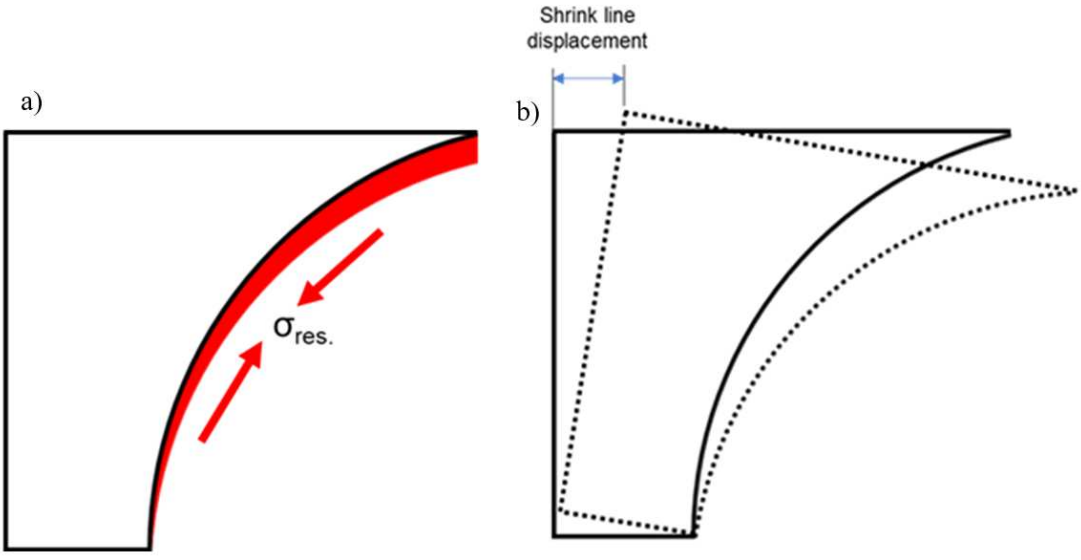

Figure 12. a) Residual stress accumulation due to over melting b) Shrink line formation during contraction

It is evident from Figure 13 that shrink line formation occurs at cross-sectional area changes on the upper surfaces of the holes. It is known that a higher cross-sectional area leads to increased energy input to the corresponding layer and part. Furthermore, the input heat energy is not effectively transferred to the previous layers due to the geometry of the upper portion of the hole and the thermal conductivity of the powder [30].

To determine a threshold value, the total cross-sectional areas at z = 9.169 mm, where the first shrink line was observed, and at four lower layers (z = 9.119 mm, z = 9.069 mm, z = 9.019 mm, and z = 8.969 mm, with a layer thickness of 0.05 mm) were measured on the geometry, as illustrated in Figure 13. The corresponding cross-sectional areas and the percentage increase in cross-sectional areas between successive layers are presented in Table 4.

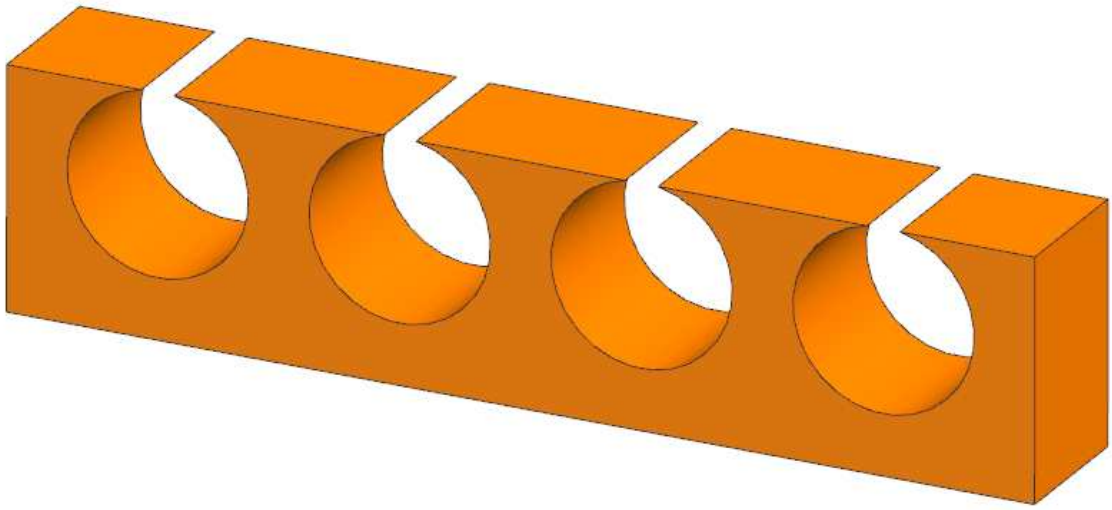

Figure 13. Cross-sectional area measurements at lower layers of area where the first shrink line was observed

Table 4. Cross-sectional areas and percent increase in cross-sectional areas between successive layers

Z Heights (mm)	**Cross-sectional areas (mm^2)**	**Percent increase in cross-sectional areas between successive layers (%)**
8.969	126.8	-
9.019	132.5	4.5
9.069	139.2	5.1
9.119	148.1	6.4

9.169	170.0	14.8

It is evident from Table 4 that the shrink line phenomenon was not observed at cross-sectional area changes of less than approximately 15%. However, when the cross-sectional area changed from 148.1 mm² to 170.0 mm² at z = 9.119 mm and z = 9.169 mm, respectively, this sudden cross-sectional area change (14.8%) resulted in shrink line formation. Therefore, it can be concluded that sharp cross-sectional area changes exceeding 15% should be avoided during the design process to eliminate shrink line formation in the PBF-LB/M process. It should be noted that this threshold value is based solely on cross-sectional area changes. If additional parameters, such as perimeter, centroids of islands, or other related factors, were included in the evaluations, the threshold value would likely change, as stated in Ref [10].

3.2. Build Simulation Results

The total and X-axis displacement results are presented in Figure 14. The comparison between the simulation and experimental data points is shown in Figures 15 and 16. The build simulation results accurately predicted the shrink line depths and z-heights for both sidewalls, as seen in Tables 5 and 6, and Figure 17. The divergence between the build simulation and experimental results is less than 1.3% for shrink line z-coordinate locations and less than 28.1% for shrink line depths. The build simulation predicted higher shrink line depths compared to the experimental results. Additionally, the measurement results indicate varying shrink line depths on different sides of the specimens. This discrepancy can be attributed to the recoater and gas flow direction.

As previously mentioned, the high thermal gradients at sharp cross-sectional area changes cause the melt pool to penetrate towards the sides of the features or parts, which is captured by the simulation as displacement. It is worth noting that the simulation results clearly identify the shrink line locations, which are in strong agreement with the experimental results, with a divergence of less than 1.3%. The use of a finer voxel element size (0.1 mm) in this study, as determined through the mesh convergence study, significantly contributes to the high accuracy of simulating the height of the shrink lines.

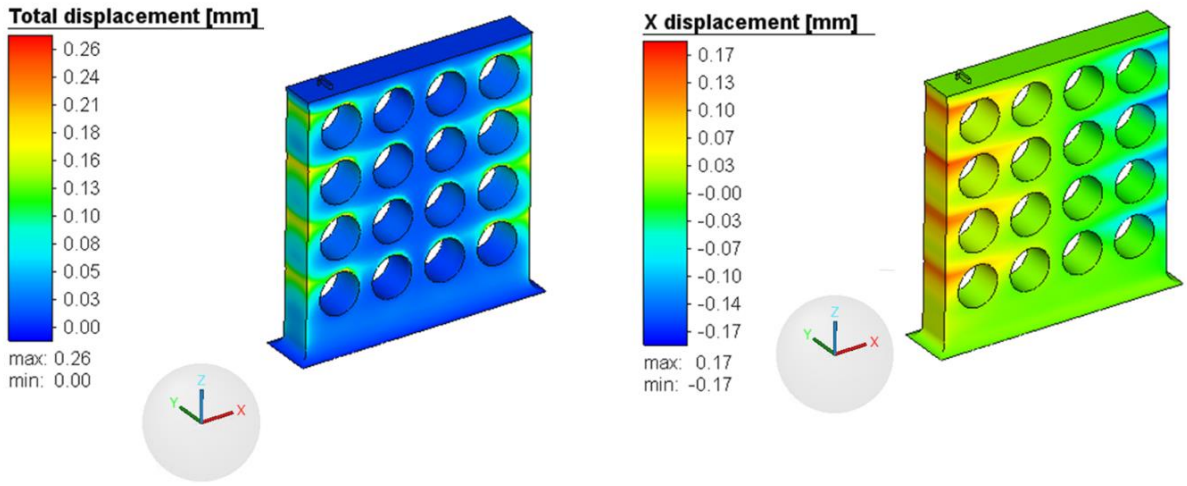

Figure 14. FEM simulation results of total (left) and X axis (right) displacement results from surface

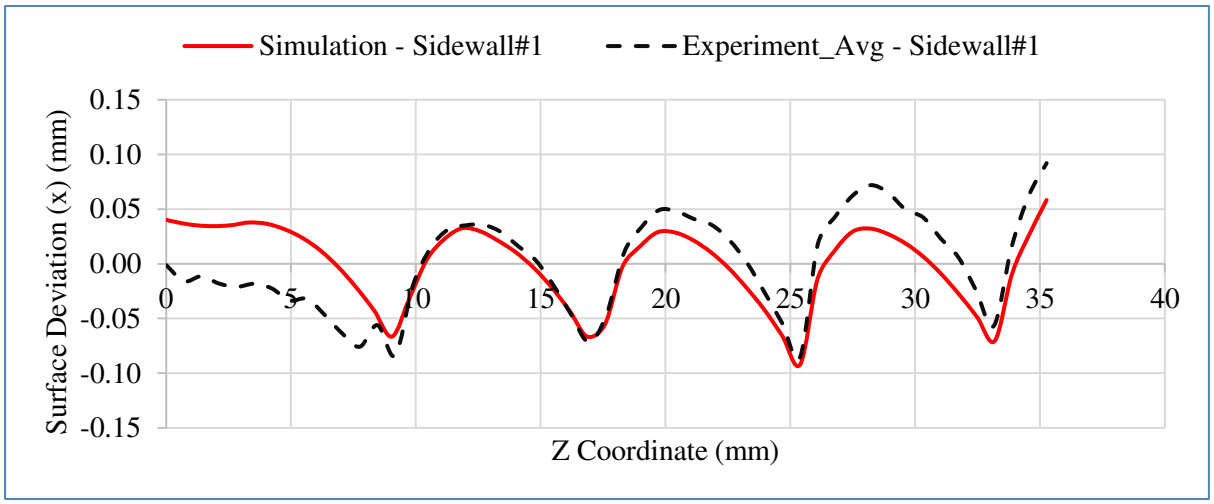

Figure 15. The comparison of experimental and simulation results for left side wall

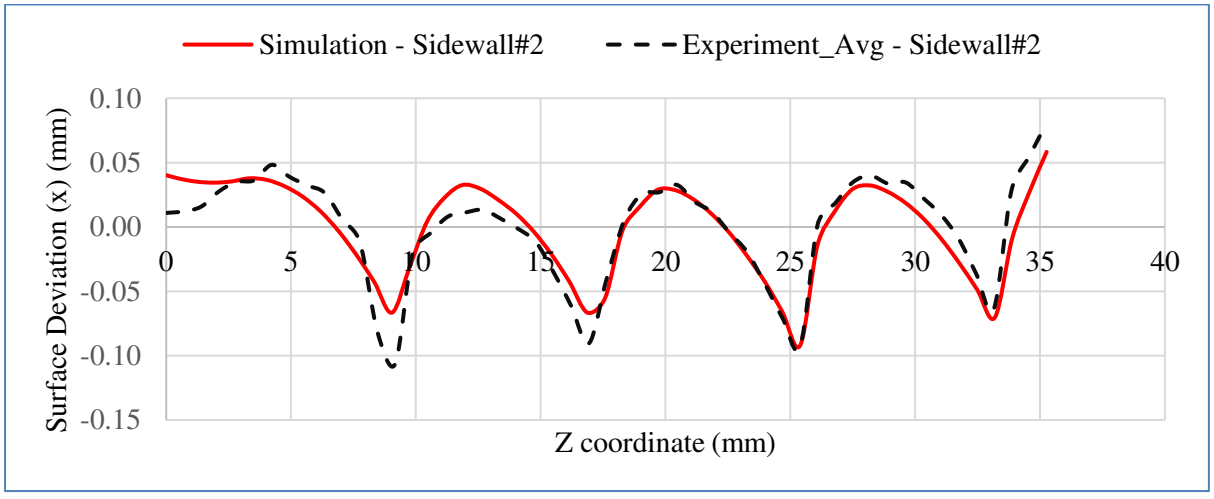

Figure 16. The comparison of experimental and simulation results for right side wall

Table 5. Shrink line z-coordinate comparison with simulation results. Values are in mm.

	Shrink Line#1	Shrink Line#2	Shrink Line#3	Shrink Line#4
Experiments	9.169	16.927	25.390	33.148
Simulation	9.047	16.868	25.395	33.188
Divergence	+1.3%	+0.4%	-0.02%	-0.1%

Table 6. Shrink line depth comparison with simulation results. Values are in mm.

	Shrink Line#1	Shrink Line#2	Shrink Line#3	Shrink Line#4
Front Sidewall Experiment_Avg	0.120	0.121	0.157	0.149
Back Sidewall Experiment_Avg	0.120	0.123	0.133	0.145
Simulation	0.099	0.096	0.124	0.129
Divergence	+21.2%	+28.1%	+26.6%	+15.5%

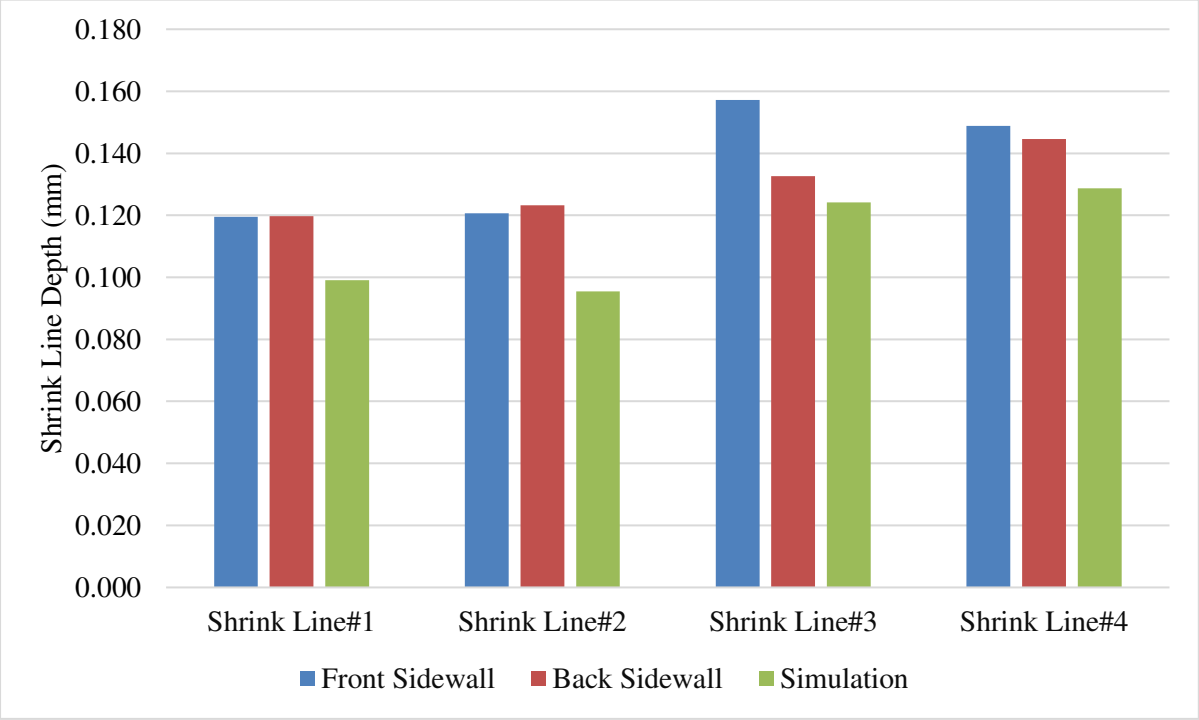

Figure 17. Shrink line depth comparison with simulation

From the results, it can be concluded that the developed method is capable of predicting the location of the shrink line with an error margin of less than 1.3%. Additionally, the shrink line

depths can be predicted with an error range between 15.5% and 28.1%, resulting in an average error of 22.9%.

3.3. Microstructure and Microhardness Measurement Results

Microhardness measurements were conducted on the lateral polished surfaces along four shrink lines and the areas between them. The corresponding measurement areas are illustrated in Figure 18. At each of these areas, five microhardness measurements were performed, and their averages are presented in Table 7. For zones 1 through 5, microhardness measurements were taken at 0.5 mm above or below the shrink line locations.

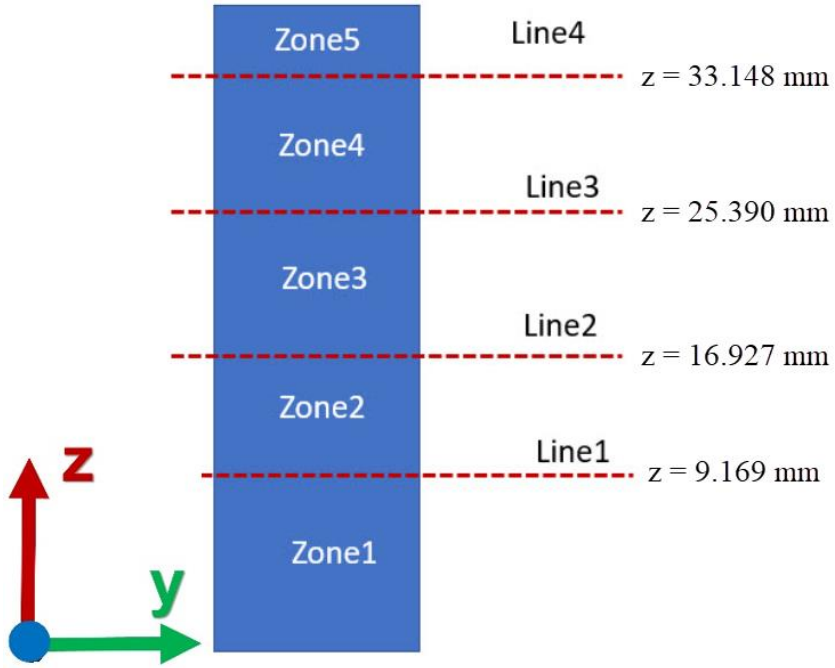

Figure 18. Microhardness measurement areas

Table 7. Microhardness measurement results

Area	Microhardness (HV)
Line 1	302.8 ± 6.1
Line 2	306.4 ± 6.1
Line 3	313.8 ± 6.3
Line 4	296.4 ± 5.9
Zone 1	307.0 ± 6.1

Zone 2	316.4 ± 6.3
Zone 3	314.2 ± 6.3
Zone 4	302.0 ± 6.0
Zone 5	323.7 ± 6.5

Hardness is influenced by factors such as potential subsurface defects, grain size, local cooling rates, or additional heating from subsequent layers. As shown in Table 7, microhardness at shrink line locations is slightly lower than in the surrounding areas, except for the shrink line at location 3. For example, the microhardness at shrink line location 1 (302.8 HV) is lower than the microhardness at the lower zone (Zone 1, 307.0 HV) and the upper zone (Zone 2, 316.4 HV). This can be attributed to the reduced presence of partially melted particles at shrink line locations, where the melt pool is formed by fully melted powder particles due to high energy input [30]. Additionally, fewer partially melted particles are attached at the shrink line location, resulting in lower microhardness compared to the surrounding areas. This phenomenon is also evident in the SEM images.

SEM images for one of the shrink lines (z = 16.927 mm) are shown in Figure 19. It is clear that the reduced attachment of partially melted particles to the shrink line surface indicates higher energy input, which melts more powder and introduces higher heat cycles that promote coarser grains. This may be attributed to the geometrical shifting of the shrink line. In other words, as the shrink line pulls inward along the x-direction, it moves away from the powder (due to residual stress and/or shrinkage), causing the next layer to interact with less powder during laser melting. Various studies have also reported phenomena such as melt pool sagging and partially melted powder adhesion [29, 31]. Furthermore, the microstructure of the zones and shrink lines was examined using SEM, and no significant differences were observed, as indicated in Ref [9].

It is well known that the melt pool formed during printing can be divided into three zones: the core zone, where the microstructure is fine; the coarse zone, which is the boundary between the core zone and the heat-affected zone (HAZ) and contains a coarser microstructure; and finally, the HAZ, which is the outer boundary of the melt pool [32]. Various studies have also indicated that the coarsened microstructure in the melt pool, caused by prolonged exposure to high temperatures, leads to a decrease in microhardness [33–34]. Due to the high thermal

gradients at shrink line locations, the microstructure at these locations becomes coarser, resulting in a reduction in microhardness.

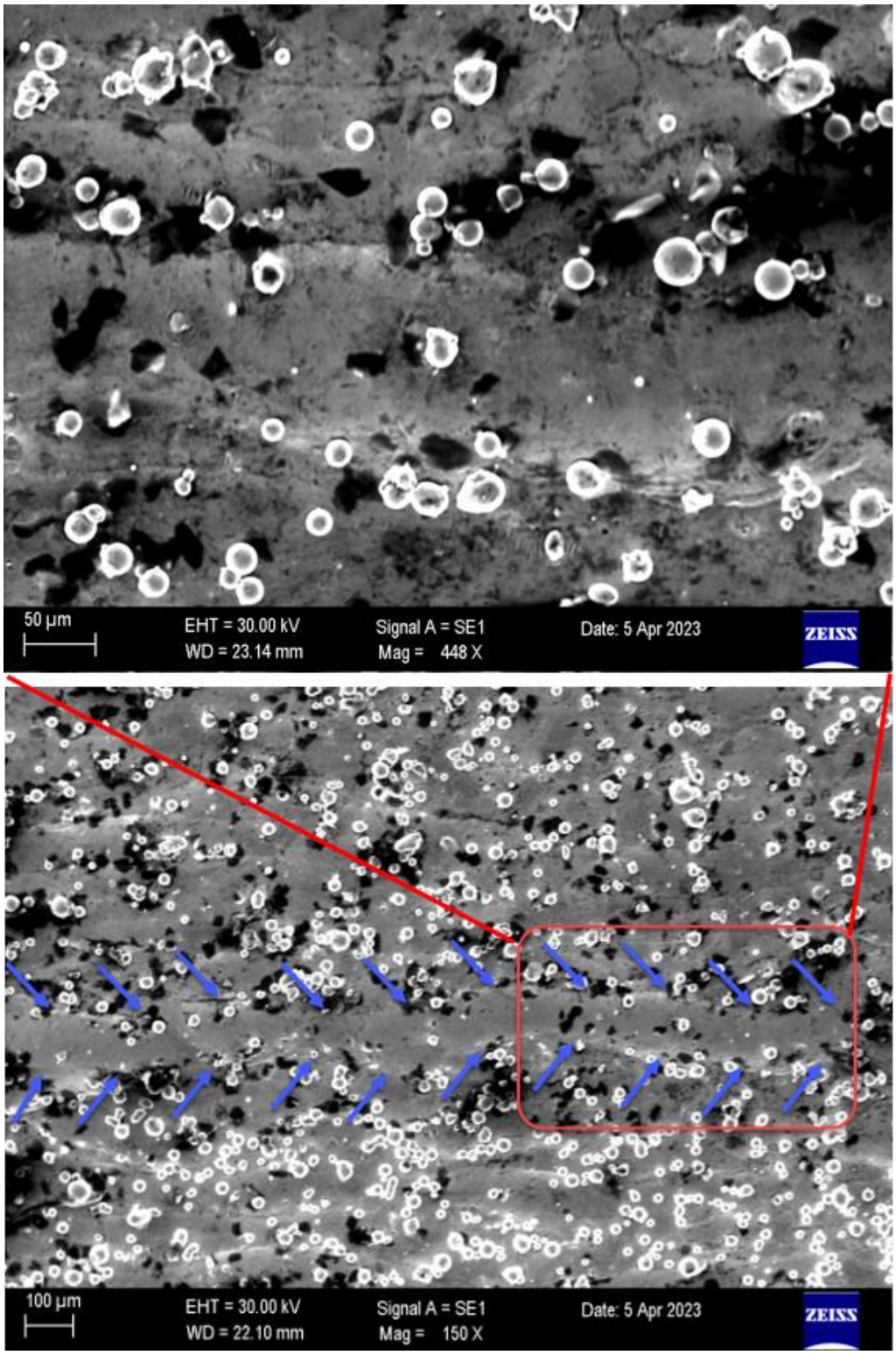

Figure 19. SEM images for the shrink line at z = 16.927 mm (blue arrows show the shrink line boundary)

4. Conclusions

This study examined the shrink line formation characteristics of PBF-LB/M printed parts with sharp geometrical transitions, leading to the emergence of a noticeable line on their surface. This line represents a dimensional change at the specific layer where the geometrical transition occurs. The effect of the shrink line on the part can result in reduced mechanical performance, which is influenced by the extent of the geometric shift caused by the sharp transition. While no observable alteration in the internal structure of the object is detected at the shrink line location, explicit differences are observed on the surface of the part in the shrink line region. Additionally, a numerical method was employed to predict the shrink line formation, including its size and location. The main findings of the study can be summarized as follows:

- In the patterned hole features, shrink line formation was observed at cross-sectional area changes on the upper surfaces of the holes, where the cross-sectional area changes exceeded 15%. This value may be considered a threshold during the design process.
- Voxel element size is a critical factor in simulation, as it creates a tradeoff with computational time. In the present study, the use of a low voxel element size allowed the simulation to accurately predict shrink lines; however, shrink lines were not observed when higher element sizes were used.
- The divergence between the build simulation and experimental results is less than 1.3% for shrink line z-coordinate locations and less than 28.1% for shrink line depths.
- Fewer partially melted particles attached to the shrink line surface indicate a higher energy input, which melts more powder and introduces higher heat cycles that promote the formation of coarser grains.
- Microhardness at shrink line locations was found to be approximately 2–9% lower than that of the surrounding areas.
- The measurement deviation of shrink line z-heights and depths was calculated, revealing that the z-heights of shrink lines remain consistent without deviation; however, shrink line depths vary between 1.65% and 15%.
- The z-heights of the shrink lines are consistent in both the front and back sidewalls, indicating that the shrink occurs in the same layer of the part. However, the depth of the shrink lines is greater on the sidewalls that first encounter the recoater blade.

- As part of future studies, the location and depth of the shrink line will be determined analytically, complemented by metallographic inspections to assess the characteristics of the shrink line.

Declarations

a. Funding

This work was supported by the The Scientific and Technological Research Council of Türkiye (TÜBİTAK) (no. 5158001).

b. Conflicts of interest

The authors declare no competing interests.

c. Authors' contribution

Kadir Gunaydin: conceptualization, data curation, formal analysis, investigation, methodology, validation, visualization, writing—original draft, writing—review and editing. Erdem Kundakçıoğlu: data curation, formal analysis, methodology. Orhan Gülcan: data curation, writing—original draft, writing—review and editing. Evren Yasa: conceptualization, data curation, formal analysis, methodology, supervision, validation, visualization, writing—review and editing.

References

[1] Gong G, Ye J, Chi Y, Zhao Z, Wang Z, Xia G, Du X, Tian H, Yu H, Chen C (2021) Research status of laser additive manufacturing for metal: a review. J Mater Res Technol 15: 855-884. https://doi.org/10.1016/j.jmrt.2021.08.050.

[2] Fateri M, Gebhardt A (2021) 3D printing of optical components – introduction to additive manufacturing. Cham: Springer International Publishing. pp 1–22.

[3] Kruth JP (1991) Material incress manufacturing by rapid prototyping techniques. CIRP Annals 40(2): 603–614. https://doi.org/10.1016/S0007-8506(07)61136-6

[4] Yadroitsev I, Yadroitsava I, Du Plessis A (2021) Basics of laser powder bed fusion. In: Yadroitsev I, Yadroitsava I, du Plessis A, MacDonald E (ed) Additive manufacturing materials and technologies, fundamentals of laser powder bed fusion of metals, Elsevier, pp 15-38. https://doi.org/10.1016/B978-0-12-824090-8.00024-X.

[5] Morvayová, A, Contuzzi, N, Casalino, G (2023) Numerical prediction of lack-of-fusion defects in selective laser melted AlSi10Mg alloy. Mater Sci Technol 39(16): 2334-2340. https://doi.org/10.1080/02670836.2023.2198889.

[6] Bartlett JL, Li X (2019) An overview of residual stresses in metal powder bed fusion. Addit Manuf 27: 131-149. https://doi.org/10.1016/j.addma.2019.02.020

[7] Mercelis P, Kruth JP (2006) Residual stresses in selective laser sintering and selective laser melting. Rapid Prototyp J 12: 254-264. https://doi.org/10.1108/13552540610707013

[8] Zaeh M, Branner G (2009) Investigations on residual stresses and deformations in selective laser melting. Prod Eng 4: 35–45. https://doi.org/10.1007/s11740-009-0192-y.

[9] Richardsen S, Crawford G, Gockel J (2023) Effect of a build pause on the fatigue behavior of laser powder bed fusion 316L stainless steel with as-build surfaces. Eng Fail Anal 153: 107590. https://doi.org/10.1016/j.engfailanal.2023.107590.

[10] Rauner D, Wenzler D L, Wolf D, Granz F, Zaeh MF (2024) Experimental investigations on the formation mechanisms of shrink lines in powder bed fusion of metals using a laser beam. Adv Ind Manuf Eng 9: 100149. https://doi.org/10.1016/j.aime.2024.100149.

[11] Goetz D, Wolf D, Lehmann M, Zaeh MF (2022) A novel approach for the quantitative characterization of shrink lines in the Powder Bed Fusion of metals using a laser beam. Procedia CIRP 111: 832-837. https://doi.org/10.1016/j.procir.2022.08.093.

[12] Deradjat D, Minshall T (2017) Implementation of rapid manufacturing for mass customisation. J Manuf Technol Manag 28(1): 95–121. https://doi.org/10.1108/JMTM-01-2016-0007

[13] Adam GAO, Zimmer D (2014) Design for Additive Manufacturing—Element transitions and aggregated structures. CIRP J Manuf Sci Technol 7 (1): 20-28. https://doi.org/10.1016/j.cirpj.2013.10.001.

[14] Kranz J. (2017) Methodik und Richtlinien fuer die Konstruktion von laser additiv gefertigten Leichtbaustrukturen. Springer Vieweg, Berlin, Heidelberg.

[15] Goetz, D, Diller, J, Achatz, K, Zaeh, MF (2024) Shrink line impact on the fatigue resistance of Inconel 718 parts manufactured by powder bed fusion of metals using a laser beam. J Manuf Process 115: 481-490. https://doi.org/10.1016/j.jmapro.2024.02.030

[16] Rauner D, Wolf D, Spano L, Zaeh M F (2024) A method for the predictive and automated detection of the shrink line location during the powder bed fusion of metals using a laser beam. Procedia CIRP 126: 561-566. https://doi.org/10.1016/j.procir.2024.08.240.

[17] Gülcan O, Gunaydin K, Simsek, U (2024) A numerical investigation about shrink line formation in TPMS lattice structures during LPBF process. MATİM. 22(1):8-16. https://doi.org/10.56193/matim.1370140

[18] Schnabel K, Baumgartner J, Möller B, Scurria M (2021) Fatigue assessment of additively manufactured AlSi10Mg structures using effective stress concepts based on the critical distance approach. Weld World 65: 2119–2133. https://doi.org/10.1007/s40194-021-01153-9.

[19] Kranz F, Herzog D, Emmelmann C (2015) Design guidelines for laser additive manufacturing of lightweight structures in TiAl6V4. J Laser Appl 27: S14001. https://doi.org/10.2351/1.4885235

[20] Herzog D, Asami K, Scholl C, Ohle C, Emmelmann C, Sharma A, Markovic N, Harris, A (2022) Design guidelines for laser powder bed fusion in Inconel 718. J Laser Appl 34: 012015. https://doi.org/10.2351/7.0000508

[21] Contuzzi, N, Sabina L C, Fabrizia C, and Vittorio A (2019) Design and fabrication of random metal foam structures for laser powder bed fusion. Materials 12 (8): 1301. https://doi.org/10.3390/ma12081301.

[22] Denlinger E R, Gouge M, Irwin J, Michaleris P (2017) Thermomechanical model development and in situ experimental validation of the Laser Powder-Bed Fusion process. Addit Manuf 16: 73-80. https://doi.org/10.1016/j.addma.2017.05.001.

[23] Gouge M, Michaleris P, Denlinger E, Irwin J (2018) The finite element method for the thermo-mechanical modeling of additive manufacturing processes. In Gouge M, Michaleris P (ed) Thermo-mechanical modeling of additive manufacturing, Butterworth-Heinemann. pp 19-38. https://doi.org/10.1016/B978-0-12-811820-7.00003-3.

[24] Zhang T, Yuan L (2022) Understanding surface roughness on vertical surfaces of 316 L stainless steel in laser powder bed fusion additive manufacturing. Powder Technol 411: 117957. https://doi.org/10.1016/j.powtec.2022.117957.

[25] Fox JC, Moylan SP, Lane BM (2016) Effect of process parameters on the surface roughness of overhanging structures in laser powder bed fusion additive manufacturing. Procedia CIRP 45: 131-134. https://doi.org/10.1016/j.procir.2016.02.347.

[26] Snyder JC, Thole KA (2020) Understanding laser powder bed fusion surface roughness. J Manuf Sci Eng 142 (7): 071003. https://doi.org/10.1115/1.4046504.

[27] Morvayova, A, Fabbiano, L, Contuzzi, N, Caiazzo, F, & Casalino, G (2023) On the influence of building position on dimensional accuracy and surface quality of aluminum blocks manufactured by L-PBF. Opt Laser Technol 167: 109830. https://doi.org/10.1016/j.optlastec.2023.109830

[28] Wang Z, Stoica, AD, Ma D, Beese AM (2018) Stress relaxation in a nickel-base superalloy at elevated temperatures with in situ neutron diffraction characterization: Application to additive manufacturing. Mater Sci Eng A 714: 75-83. https://doi.org/10.1016/j.msea.2017.12.058.

[29] Denlinger ER, Heigel JC, Michaleris P (2014) Residual stress and distortion modeling of electron beam direct manufacturing Ti-6Al-4V. Proc Inst Mech Eng B: J Eng Manuf 229 (10): 1803–1813. https://doi.org/10.1177/0954405414539494.

[30] Kundakcıoğlu E, Lazoglu I, Poyraz Ö, Yasa E, Cizicioğlu N (2018) Thermal and molten pool model in selective laser melting process of Inconel 625. Int J Adv Manuf Technol 95: 3977-3984. https://doi.org/10.1007/s00170-017-1489-1.

[31] Kundakcıoğlu E, Lazoglu I, Poyraz Ö, Yasa E (2022) Modeling of residual stress and distortion in direct metal laser sintering process: a fast prediction approach. Prod. Eng. Res. Devel. 16: 769-783. https://doi.org/10.1007/s11740-022-01135-w.

[32] Gulcan O, Gunaydın K, Celik A, Yasa E (2027) Mechanical properties of laser powder bed fusion produced overhang parts with different support geometries: an experimental study. Prog Addit Manuf 9:211-229. https://doi.org/10.1007/s40964-023-00443-6.

[33] Bartolomeu F, Dourado N, Pereira F, Alves N, Miranda G, Silva FS (2020) Additive manufactured porous biomaterials targeting orthopedic implants: A suitable combination of mechanical, physical and topological properties. Mater Sci Eng C 107: 110342. https://doi.org/10.1016/j.msec.2019.110342.

[34] Bartolomeu F, Fonseca J, Peixinho N, Alves N, Gasik M, Silva FS, Miranda G (2019) Predicting the output dimensions, porosity and elastic modulus of additive manufactured biomaterial structures targeting orthopedic implants. J Mech Behav Biomed Mater 99: 104-117. https://doi.org/10.1016/j.jmbbm.2019.07.023.